Durable Cr-substituted $(Ba,Cs)_{1.33}(Cr,Ti)_8O_{16}$ hollandite waste forms with high Cs loading

Mingyang Zhao,[a†] Nancy Birkner,[a†] Joseph Schaeperkoetter,[c] Robert J. Koch,[c] Patrick Russell,[a] Scott T. Misture,[c] Theodore Besmann,[d] Jake Amoroso,[*b] Kyle Brinkman[*a]

[a]Department of Materials Science and Engineering, Clemson University, Clemson, SC 29634, USA.

[b]Savannah River National Laboratory, Aiken, SC 29808, USA.

[c]Kazuo Inamori School of Engineering, Alfred University, Alfred, NY 14802, USA.

[d]Nuclear Engineering Program, Department of Mechanical Engineering, University of South Carolina, Columbia, SC 29208, USA.

[†]These authors contributed equally to this work.

[*]Co-corresponding author Tel and email. Tel: +1(864) 656-1405; Email: ksbrink@clemson.edu (Kyle Brinkman); Jake.Amoroso@SRNL.DOE.gov (Jake Amoroso)

Abstract

A series of Cr-substituted hollandite solid solution $Ba_xCs_yCr_{2x+y}Ti_{8-2x-y}O_{16}$ over a broad range of Cs content ($x + y = 1.33$, $0 \leq x$ and $y \leq 1.33$) were systematically investigated. A monoclinic-to-tetragonal phase transition was induced by increasing Cs content in the tunnel sites of the hollandite structure, and all members of the series show structure modulations related to the ordering of the Ba/Cs and vacancies along the tunnels. The thermodynamic stability of the Cr-substituted hollandite samples was measured via high-temperature oxide

This article has been accepted for publication and undergone full peer review but has not been through the copyediting, typesetting, pagination and proofreading process, which may lead to differences between this version and the Version of Record. Please cite this article as doi: 10.1111/jace.18419.

melt solution calorimetry which included making the first measurements of the enthalpies of drop solution for Cs_2O and BaO in sodium molybdate solvent at 800 °C. Thermodynamic stability increased with increasing Cs content for the series of Cr-substituted hollandite, which also exhibited a greater thermodynamic stability compared to other substituted hollandite analogs including Zn, Ga, Fe, and Al variants. The leaching performance, also known as aqueous durability, demonstrated that the fractional Cs release in the Cr hollandite samples is much lower than in other hollandite systems. After seven days of leaching at 90 °C, the lowest Cs release was observed in the sample with the highest Cs content, approximately 22 wt.% Cs. The Cs release could be further suppressed, by approximately 3x if the sample was further densified and sintered. The Cs release results correlated inversely to the thermodynamic stability, suggesting that the thermodynamic stability may be used in future materials design for nuclear waste immobilization.

1. Introduction

Currently, borosilicate glass is the most accepted waste form for the long-term disposition of high-level waste (HLW).[1] Borosilicate glass can effectively immobilize a broad range of radioactive (and non-radioactive) elements present in HLW and exhibits excellent chemical durability in an aqueous environment. While borosilicate glass is the standard waste form, one limitation to its expanded use is the relatively inferior thermal stability of glasses to crystalline materials. During the decay of radionuclides with short half-lives (e.g., ^{90}Sr and ^{137}Cs),[2] heat is released, which, if those radionuclide concentrations are sufficient, can raise the internal temperature of the glass causing it to potentially devitrify or exhibit increased elemental release, especially when several thousand HLW glass canisters are aggregated in an underground repository.[3–7] In practice, the decay heat is controlled during the vitrification

process through limits placed on the watt output per canister. In addition, self-irradiation that occurs in nuclear waste glasses can also induce potential devitrification.[8] These drawbacks place a limitation on the application of borosilicate glass.

Several crystalline ceramic candidates have been proposed as alternatives to vitreous nuclear waste forms for their relatively higher thermal stability. In the late 1970s, Ringwood and coworkers[7] developed a multiphase ceramic, SYNROC, to immobilize high-level waste (HLW). SYNROC is designed using existing mineralogy and knowledge of durable crystalline materials found in nature. The hollandite mineral group is one of the most studied as a template for SYNROC materials which include the titanate mineral forms of hollandite, perovskite, and zirconolite. For example, in a multi-phase waste form designed to immobilize a mixed waste stream, hollandite is targeted to accommodate fission products such as Cs, Ba, and Rb, perovskite is targeted to capture Sr, and various actinides (e.g., U and Th) and Zr can be incorporated into zirconolite.[7, 9, 10] The difficulty to incorporate and immobilize Cs in a phase that is durable at elevated temperatures and in aqueous conditions, has been the foundation for significant research efforts to design and fabricate hollandite materials with improved performance.

The long-term (e.g., millennia) stability of a waste matrix is directly related to its thermodynamic stability and resistance to elemental dissolution. According to previous studies on hollandite-type materials,[11–15] thermodynamic stability was found to be correlated to the Cs content and increased with increasing Cs content. Moreover, the higher stability compositions exhibited correspondingly less Cs release after exposure to accelerated leach testing. Recent results indicated that Cr-substituted hollandite forms with high phase purity and exhibits lower Cs release rates relative to other substituted hollandites.[16–18] Although numerous hollandite series with different substitutions (e.g., Zn^{2+}, Al^{3+}, Ga^{3+}, and Fe^{3+}) have been investigated, thermodynamic and leaching data of the Cr-substituted hollandite is

limited. In this work, a series of single-phase Cr-substituted hollandite samples with varying Cs content were synthesized. Structural evolution, thermodynamic stability, and elemental leaching rate were measured as a function of the Cs content and compared to Zn-, Ga-, Fe-, and Al-substituted hollandite series. These results are discussed in the broader context of available data for the other hollandite systems to provide a comprehensive perspective and help guide future materials design of crystalline ceramic materials for nuclear waste immobilization.

2. Materials and methods

2.1 Sample synthesis

The series of Cr-substituted hollandite $Ba_xCs_yCr_{2x+y}Ti_{8-2x-y}O_{16}$ ($0 \leq x \leq 1.33$; $x + y = 1.33$) was synthesized via solid-state reactions. For simplicity, they are denoted as HCy in this manuscript. "H", "C", and the value of "y" refer to "Hollandite", "Cr", and "Cs content", respectively. For example, the target formula of the sample HC0.33 is $Ba_1Cs_{0.33}Cr_{2.33}Ti_{5.67}O_{16}$. The target stoichiometries and the short names of the Cr-substituted hollandite samples are listed in Table 1.

Two sample sets were synthesized: one at Clemson University (CU) and another at Savannah River National Laboratory (SRNL). General experimental procedures are described as follows: Reagent-grade powders of barium carbonate, $BaCO_3$, cesium carbonate, Cs_2CO_3, chromium (III) oxide, Cr_2O_3, and titanium oxide (anatase), TiO_2, were used as starting materials without drying. Stoichiometric amounts of raw materials were placed into high-density polyethylene (HDPE) bottles. Ethanol or DI water and spherical yttrium stabilized zirconia (YSZ) grinding media (diameter: 5 mm and/or 10 mm) were added into the bottles to mix the powders. Ball-milling was performed for more than 20 min to obtain a homogenous

slurry, subsequently dried in an oven. The resulting batch material was further processed according to the following:

For the samples synthesized at CU, the batch material was cold-pressed into pellets at ~250 MPa. Multiple heat treatment processes were completed in a high-temperature box furnace as follows: (1) the pellets were heated to 1000 °C for 5 h to decompose the carbonates; (2) the post-calcination pellets were crushed, ground, and wet ball-milled; (3) as-obtained slurry was dried in an oven at 80 °C; (4) as-dried powders were ground, pressed and fired between 1200 °C - 1250 °C for 10 h. Alumina crucibles were used and covered with alumina lids.

For the samples synthesized at SRNL, the batch material was calcined in covered Pt/10Rh crucibles at 1000 °C for 20 min and then removed from the furnace to cool down to room temperature (RT). After cooling, the materials were ground in a pulverizer (Angstrom) for 2 min, returned to the same crucible with the lid, and heated from RT to 1450 °C. After 20 min dwelling at 1450 °C, the crucible was removed from the furnace to air cool.

2.2 Characterization

Powder X-ray diffraction (XRD) measurements were performed to analyze the phase purity and crystal structures of as-synthesized samples. A Rigaku Miniflex600 diffractometer (40 kV and 15 mA) with monochromatic Cu Kα radiation (λ = 1.5406 Å) was used to collect the diffraction patterns for phase ID, and a Bruker D8 with Lynxeye XE detector was used to collect the wide-range data for Rietveld refinements and modulated structure analysis.

Synchrotron-based powder XRD was also used to characterize a subset of samples, with the data reported herein collected at the Advanced Photon Source beamline 11-ID-B at a wavelength of 0.1430 Å. The samples were contained in 1.1 mm diameter polyimide capillaries and measured under ambient conditions using a Perkin Elmer amorphous Si 2-D

detector and Debye-Scherrer geometry. The sample-to-detector distance used for the PXRD measurements was 950 mm, yielding a d-spacing range of ~19 to 0.55 Å.

The microstructure of samples was observed by SU6600 scanning electron microscopy (SEM). Elemental compositions were analyzed by energy-dispersive X-ray spectroscopy (EDS) using Aztec software (Oxford Instruments). The EDS compositions listed in Table 1 were determined by averaging the compositions of at least eight representative sites over the surfaces of the samples. Chemical compositions of the samples and leachate solutions were measured with inductively coupled plasma-mass spectroscopy (ICP-MS). A lithium metaborate fusion preparation with nitric acid digestion was used to dissolve solid samples for ICP-MS.

Table 1.

2.3 High-temperature oxide melt solution calorimetry

Formation enthalpies are fundamental thermodynamic properties that define phase stability. The standard enthalpy of formation, as well as the enthalpy of formation from oxides, is the energy associated with the reaction to form the compound from its component elements or oxides. Calorimetry provides the only direct method by which formation enthalpy is experimentally measured. The total heat effect (ΔH_{ds}) includes the heat of solution (ΔH_{sln}) and the heat content of the sample (ΔH_T). Calibration is done against the known heat content of trace metal grade alpha-alumina (Sigma Aldrich, 99.999%). The calibration and experiment methodologies are described in detail elsewhere.[19, 20]

In this work, calorimetric measurements were done using high-temperature oxide melt solution calorimetry with an AlexSYS 1000 (Seteram Inc.) isoperibol Calvet twin calorimeter. Hand-pressed sample pellets weighing between 4-6 mg were dropped from RT into a platinum crucible containing 20.00 ± 0.05 g molten sodium molybdate solvent

($3Na_2O{\cdot}4MoO_3$) at ~800 °C within the calorimeter. Oxygen was flushed through the glassware assembly at 30 mL/min and bubbled through the solvent at 2.5 mL/min. Flushing ensures constant vapor pressure above the solvent while bubbling aids dissolution. To obtain the mean enthalpy of drop solution (ΔH_{ds}), experiments were replicated at least eight experiments per sample composition to achieve statistically reliable data. Uncertainties were computed as twice the standard deviation of the mean. Measurements were only performed on the CU sample set based on thermodynamically similar states considering ceramic crystallization kinetics.

The values of ΔH_{ds} of the binary oxides (e.g., BaO, Cs_2O, Cr_2O_3, and TiO_2) that form the Cr hollandite samples are required to apply the appropriate thermochemical cycle used for the calculation of the formation enthalpies from the constituent oxides. Cr_2O_3 and TiO_2 have been previously measured and reported, however, the ΔH_{ds} of BaO, Cs_2O were unknown. Cs_2O and BaO are very hygroscopic making them unstable resulting in inconsistent drop solution data. For this reason, Cs_2CO_3 and $BaCO_3$ (99.99 %, Sigma Aldrich) were dried and then maintained at 300 °C before calorimetric measurements.

2.4 Leaching tests

Aqueous leaching tests following the ASTM C1285 Product Consistency Test (PCT) Method-B standardized protocol were performed to measure elemental release.[21] Samples were ground and sieved to –100/+200 mesh, washed with water and alcohol, and then dried. Before the leaching test, sub-samples of the washed particles were dissolved and measured for chemical composition with ICP-MS. For the leaching test, 10 mL of deionized water (leachate) for 1 g of sample was prepared to maintain a constant V_{water}/m_{sample} ratio of 10 mL/g. Samples and one reference were prepared in triplicate along with two blanks. Tests were performed in stainless-steel (SS) vessels, closed, sealed, and placed in an oven at 90 ± 2 °C for seven days. Once cooled down to room temperature, the leachate solution was

analyzed by mass spectrometry. The fractional release of element *i* in the measured samples, was calculated using Equation 1:

$$FR_i = \frac{C_i V}{m_s f_i} \quad (1)$$

where FR_i = fractional release of element *i* (dimensionless), C_i = concentration of element *i* in the leaching solutions (g/L), V = volume of the leaching solution (L), m_s = mass of the measured sample (g), and f_i = mass fraction of element *i* in the measured sample (dimensionless).

3. Results and discussion

3.1 Phase, microstructure, and composition

The X-ray diffraction patterns and lattice information refined by the Rietveld method are given in Figure 1 and Table 2 for the series of the Cr-substituted hollandite samples synthesized as $Ba_xCs_yCr_{2x+y}Ti_{8-2x-y}O_{16}$. As shown in Figure 1a, all samples are either pure or nearly pure hollandites with a minor $Cs_2(CrO_4)$ phase identified in HC0.67. The Ba end member (y = 0) adopts monoclinic symmetry (space group: *I*2/*m*), whereas the hollandite samples with y > 0 exhibit tetragonal symmetry (space group: *I*4/*m*). The composition-driven monoclinic-to-tetragonal (M-T) phase transition as a function of the Cs content is related to the relative size of average B-site cations to A-site cations. The boundary of this M-T phase transition was effectively predicted by Zhang and Burnham.[22] As illustrated in Figure 1c, smaller B-site cations (e.g., $R_{Al^{3+}} = 0.535$ Å) help the hollandite remain tetragonal over the entire compositional range.[14, 23] In contrast, the M-T phase transition would occur when larger B-site substitutions are selected (e.g., $R_{Zn^{2+}} = 0.74$ Å and $R_{Fe^{3+}} = 0.645$ Å).[23] The results for the Cr hollandite ($R_{Cr^{3+}} = 0.615$ Å) presented in this work, along with Zn and Fe

hollandite analogs reported in previous studies, agree well with the Zhang and Burnham prediction.[12, 13, 22, 23]

Figure 1

Table 2.

It is well-documented that hollandites display structure modulations, which cause additional superstructure reflections in electron and X-ray diffraction patterns,[24–26] generally of weak intensity and although they can be sharp and well-defined, it is common to find broad and diffuse modulation peaks.[27–29]

It is widely agreed that the additional peaks arise from the ordering of the A-site cations along the tunnel, described by a modulation vector (0,γ,0) for monoclinic or (0,0,γ) for tetragonal systems.[30–32] When described in terms of an occupancy modulation, the breadth of the superstructure peaks is claimed to arise from the intergrowth of domains with different multiplicities, m, where

$$m = \frac{1}{\gamma} \tag{2}$$

[24, 25, 33, 34], and is related to different repeat distances of the vacancy ordering. Alternatively, the A-site can also be thought of as a separate but interpenetrating lattice with identical lattice parameters orthogonal to the tunnel direction but a separate lattice parameter along the tunnel.[28] When modeled in terms of interpenetrating lattices we define both a B-site framework and an A-site substructure. The two models are related by

$$\gamma = \frac{(b_{\mathrm{f}}^{*} - b_{\mathrm{a}}^{*})}{b_{\mathrm{f}}^{*}} \tag{3}$$

where b_f^* and b_a^* are the reciprocal lattice parameters of the B-site framework and A-site along the tunnel direction, respectively. Here, the A-site cations lie on the points of the lattice with minimization of the electrostatic repulsion between A-site cations determining the ordering scheme down the tunnel. In this model, the wide peak breadth has been attributed to the limited extent of the 3-D ordering of the A-site between adjacent tunnels.[25, 28, 35, 36]

As shown in Figure 1a, the most intense superstructure reflection falls around 26-27° 2θ and is visible for all compositions, as is another peak around 22° 2θ. To understand the data further, the synchrotron powder XRD in Figure 1b was performed on a sample ($Ba_1Cs_{0.3}Cr_{2.3}Ti_{5.7}O_{16}$) prepared in the same manner as those in Figure 1a to better define the structure modulation. The details of the A-site cation ordering along the tunnel are the subject of a separate study, but Figure 1b shows the Rietveld fit with the superstructure peaks included. Table S1 shows the structure parameters derived, demonstrating large anisotropic displacement parameters for the Cs/Ba tunnel cations in the direction along the tunnel.

The superstructure peak locations can be used to define the occupancy of the tunnel sites as $\frac{b_f}{b_a}$. With two tunnels per unit cell and formula unit $Ba_xCs_yCr_{2x+y}Ti_{8-2x-y}O_{16}$, the overall occupancy becomes:

$$x + y = 2\frac{b_f}{b_a} \tag{4}$$

This occupancy calculation has frequently been reported in the literature,[27] typically in terms of the multiplicity *m*, where

$$x + y = 2\left(1 - \frac{1}{m}\right) \tag{5}$$

The equivalence of Equations 4 and 5 follows directly from Equations (2) and (3). Despite the peaks being diffuse, the occupancy values determined from the refinement of b_a agree well with the chemical compositions for all samples as shown in Table S1 and Table 3. Comparing the values of b_a and $x + y$ for the Cs and Ba end members, it is apparent that the

Cs packs more closely along the tunnel. This observation is consistent with the reports in the literature of the Cs end member having a higher upper limit on tunnel occupancy than the Ba end member for hollandites of many B-site compositions.[36]

Uniformity of the structure modulations within the polycrystalline materials, as observed in the superstructure peak widths, is in some cases a function of the cooling rate but generally can be described as a "crystallite" size or coherent domain size where the limits are along the tunnel direction or across tunnels, or both. It is clear for the Cr-substituted hollandite series in this work, where a single cooling rate was used for all samples (Table 3), that the coherent domain size of the A-site is strongly dependent on the A-site composition, with the Ba end member remaining coherent over approximately 90 Å compared to 20-30 Å for the other compositions.

Table 3.

The microstructures of the Cr-substituted hollandite specimens are displayed in Figure 2.[15] A rod-like grain shape is exhibited in all hollandite samples HC0, HC0.33, HC0.67, and HC1.33, which agrees with previous studies of similar hollandite analogs.[14, 37] No distinct secondary phases were visible in the BSE images in Figure 2. The EDS compositions of these hollandite samples were analyzed and are summarized in Table 1. The results indicate that the compositions in the samples are close to the target stoichiometries.[15]

Figure 2.

3.2 Thermodynamic stability

Tables S2 and S3 present the two thermochemical cycles used to compute the value of enthalpy of drop solution (ΔH_{ds}) for Cs_2O.[38, 39] The value of ΔH_{ds} for BaO was obtained in the same way. This methodology has been validated by Ushakov et al.[40] Table 4 summarizes the thermochemical cycles applied to calculate room temperature enthalpies of formation for the Cr-substituted hollandite samples from the constituent oxides (e.g., BaO, Cs_2O, Cr_2O_3, and TiO_2) and the constituent elements. Table 5 lists the calculated and measured thermodynamic parameters with the number of experiments given in parentheses.

Table 4.

Table 5.

The thermodynamic stability of the Cr-substituted hollandite series was evaluated based on the enthalpies of formation which were measured using high-temperature oxide melt solution calorimetry in molten sodium molybdate ($3Na_2O{\cdot}4MoO_3$) solvent at 800 °C under oxygen atmosphere. Using appropriate thermochemical cycles, the enthalpies of drop solution enthalpies (ΔH_{ds}) of the measured samples and their constituent binary oxides form the basis to calculate the enthalpy of formation from the oxides ($\Delta H_{f,ox}$) and the elements ($\Delta H_{f,el}$) at RT. The measured heat effect (i.e., ΔH_{ds}) includes the heat content of the sample pellet as it travels from RT to the calorimeter temperature plus the enthalpy of solution (ΔH_{sln}) of the sample in the solvent. Measurements were repeated to achieve statistically reliable data. Additionally, $\Delta H_{ds}(Cs_2CO_3)$ and $\Delta H_{ds}(BaCO_3)$ were measured in this work, not having been previously measured under these conditions, but necessary to the thermochemical cycles used

to calculate the enthalpies of drop solution of the constituent binary oxides, $\Delta H_{ds}(Cs_2O)$ and $\Delta H_{ds}(BaO)$.

The results from the two thermochemical cycles applied to calculate the drop solution enthalpies of corresponding oxides from their measured carbonates are $\Delta H_{ds}(Cs_2CO_3)$ = 97.65 ± 0.76 kJ/mol and $\Delta H_{ds}(BaCO_3)$ = 128.84 ± 1.52 kJ/mol. The first thermochemical cycle calculated the enthalpy of formation from the oxides ($\Delta H_{f,ox}$) of the carbonates $\Delta H_{f,ox}(Cs_2CO_3)$ = −400.2 ± 1.20 kJ/mol and $\Delta H_{f,ox}(BaCO_3)$ = −271.4 ± 2.10 kJ/mol. Then, the second used this value, along with other auxiliary thermodynamic parameters, to calculate the drop solution enthalpy of the oxides, $\Delta H_{ds}(Cs_2O)$ = −339.96 ± 1.42 kJ/mol and $\Delta H_{ds}(BaO)$ = −179.97 ± 2.59 kJ/mol. To complete these calculations, the needed standard heats of formation and heat content of auxiliary oxides and carbonates were obtained or computed from thermodynamic data reported by Robie and Hemingway,[38] unless otherwise noted. These parameters include: $\Delta H_{T(25\text{-}800\ ^\circ C)}(CO_2)$ = 37.41 kJ/mol, $\Delta^\circ H_f(CO_2)$ = −393.5 ± 0.1 kJ/mol, $\Delta^\circ H_f(Cs_2O)$ = −346.0 ± 1.2 kJ/mol, and $\Delta^\circ H_f(BaO)$ = −548.1 ± 2.1 kJ/mol. $\Delta^\circ H_f(Cs_2CO_3)$ = −1139.7 kJ/mol and $\Delta^\circ H_f(BaCO_3)$ = −1210.90 ± 2.2 kJ/mol are referred to CRC Handbook of Chemistry and Physics.[39]

The trends of formation enthalpy as a function of the Cs content for the Cr-substituted hollandite series is shown in Figure 3. The thermodynamic stability is gradually increased when higher Cs content is introduced into the tunnel sites of the hollandite structure, which agrees with the previous finding on other hollandite systems with various framework cation substitutions such as Zn, Ga, Fe, and Al. However, the values of $\Delta H_{f,ox}$ for the Cr hollandite samples are much more exothermic compared with other substitutional cations indicating greater thermodynamic stability. Moreover, the significantly improved stability could act to suppress the elemental Cs release of hollandite waste forms demonstrated in the aqueous leaching tests.

To simulate practical waste disposal, the relative phase stability between the hollandite and potential competing phase assemblages (i.e., $BaTiO_3$ perovskite phases and binary oxides) were also assessed thermodynamically by a series of chemical reactions as previously demonstrated.[11–15, 42, 43] Figure S1 shows that the reaction to form the competing perovskite phase from any of the hollandite compositions in this study is thermodynamically unfavorable. Moreover, the thermodynamic favorability of the hollandite structure increases with Cs substitution for Ba in the tunnels, which agrees well with previous studies of hollandite waste forms with different B-site dopants.[11–15]

Figure 3.

3.3 Fractional element release

Fractional release (FR) is presented to highlight the trends in the elemental release as a function of the Cs content. The absolute normalized element release (NR), measured in g/m^2, is not an appropriate manner to report the leaching data in this work because the surface area of the particles was not measured. Microscopic observation and previous Brunauer–Emmett–Teller (BET) results indicate that a solid sphere approximation for the hollandite sample particle will incorrectly estimate the surface area.[11, 12] Nevertheless, the ASTM 1285 PCT protocols were followed to maintain a consistent particle size fraction across the series of samples to enable reasonable comparisons. The fractional release of Cs (FR_{Cs}), the element (i.e., Cs-137) of the most interest with respect to hollandite waste forms, for each Cr-substituted hollandite composition was measured and reported in Figure 4. As mentioned in Section 2.1, ground and sieved particles for the leach measurements was prepared from two

sample sets: one set consisted of particles from sintered pellets (CU), while the other set consisted of particles from compacted powder (SRNL). In both data sets, the FR_{Cs} decreased with increasing Cs content. The Cs end member of the sintered pellet set was not included due to the existence of some secondary phases (e.g., TiO_2 rutile and Cs-Al-Ti-O phases), which would affect the leaching results. Nevertheless, the lowest Cs release was observed in the composition with the highest Cs content in both data sets, and was in the range of 1 to 4 × 10^{-3} ($g_{leachate}/g_{Sample}$) after seven days of aqueous leaching at 90 °C. The trend in lower Cs release with increasing Cs content is in an agreement with the thermochemistry measurements and suggests a correlation with thermodynamic stability (Figure 3).

Figure 4.

A comparison of FR_{Cs} across the data sets indicates the sintered pellet samples released 2-3 times fewer Cs compared to the compacted powder set across all compositions. The predicted FR_{Cs} could be reduced to less than 1×10^{-3} ($g_{leachate}/g_{Sample}$) after seven days of leaching based on a linear fit to the data in Figure 5a. While not understood at this time, the results indicate that pressing and sintering pellets are beneficial to the measured chemical durability in this system.

The authors have previously reported the elemental FR values for the Ga-, Fe-, Al-, and Zn-substituted hollandite series.[11–15] Figure 5(a-c) compares the FR results of the Cs, Ba, and the B-site substitutions from the Cr-substituted hollandite series with those of the Ga, Fe, Al, and Zn analogs. The data collectively show approximately three orders of magnitude difference in the FR among the different hollandite series. Recall that NR was not calculated, but the ASTM C1285 PCT protocols[21] were employed to ensure a consistent particle size fraction (and by extension surface area) across each hollandite series. The trend in FR_{Cs} as a

function of the nominal Cs content for a given hollandite series is generally consistent with the thermochemical results illustrated in Figure 3. Specifically, the lowest Cs release is observed in the Cr hollandite series which is consistent with the most negative enthalpies of formation (higher thermodynamic stability).

Figure 5.

The elemental release behavior reveals there is inconsistency in the congruency of elemental release across the analogs. For example, Ga and Fe analogs exhibit a minimum in the Cs release (at 0.67 Cs) and these analogs have a corresponding congruency in the release of the B-site cation, but not the Ba cation, with Cs. In contrast, the Al, Cr, and Zn analogs exhibit the minimum Cs release from the Cs end member (at 1.33 Cs), and Ba and Cs exhibit congruent release from the Cr and Zn analogs, whereas Al does not. This incongruent leaching might be attributed to the weaker Cs-O bond due to its higher coordination number, longer bond length, and lower bonding energy.[5, 11, 31, 44–48] Similar incongruent leaching phenomena for the elements in different lattice sites have also been reported in a variety of crystalline ceramic wasteform systems, including hollandite, pyrochlore, and perovskite structure materials.[46, 47, 49, 50] Moreover, incongruent leaching is often associated with matrix dissolution accompanied by diffusion-controlled processes.[51] However, the data presented reveals that the congruency (or incongruency) of the leaching behavior is also a function of the Cs content. This suggests a complex leaching mechanism might result from the variable Cs content that could alter the local bonding environment of the tunnel sites and the octahedra in the framework. Further studies are necessary to understand the elemental release. It is also noted that the leaching behavior would appear to be confined to the B-site substitution framework cation (and the A-site) as evidenced by the Ti leaching rate, which is profoundly lower than Cs, Ba, and any of the B-site cations (Figure S2).[50]

Figure 6.

4. Conclusions

A series of the Cr-substituted hollandite solid solutions with a broad compositional range of Cs content were synthesized. The Ba end member was monoclinic while Cs-containing phases were tetragonal. All phases had superstructure modulations as evidenced by broad but easily discernable XRD peaks. Experimental results of high-temperature oxide melt solution calorimetry established the thermodynamic stability of the Cr hollandite series to be significantly greater compared to other hollandite analogs. The superior stability of Cr-substituted hollandite samples was accompanied by relatively lower fractional Cs release as compared to other hollandite systems, which exhibit lower thermodynamic stability. Thus, a general relationship between the thermodynamic stability and elemental release was established in hollandite-based materials, which affords a new materials design parameter for hollandite-type waste forms.

Acknowledgments

The authors acknowledge the support of the Center for Hierarchical Waste Form Materials, an Energy Frontier Research Center funded by the U.S. Department of Energy, Office of Science, Basic Energy Sciences (DE-SC0016574). Use of the Advanced Photon Source at Argonne National Laboratory (beamline 11-ID-B) was supported by the U. S. Department of Energy, Office of Science, Office of Basic Energy Sciences, under Contract No. DE-AC02-06CH11357. Work conducted at the Savannah River National Laboratory was supported by the U.S. Department of Energy under Contract No. 89303321CEM000080.

References

1. Lee WE, Ojovan MI, Stennett MC, Hyatt NC. Immobilisation of radioactive waste in glasses, glass composite materials and ceramics. Adv Appl Ceram. 2006;105(1):3–12. https://doi.org/10.1179/174367606X81669
2. Ringwood AE. Safe disposal of high level nuclear reactor wastes: a new strategy. Canberra: Australian National University Press; 1978.
3. Linard Y, Yamashita I, Atake T, Rogez J, Richet P. Thermochemistry of nuclear waste glasses: an experimental determination. J Non-Cryst Solids. 2001;286(3):200–9. https://doi.org/10.1016/S0022-3093(01)00529-4
4. Wu L, Schliesser J, Woodfield BF, Xu H, Navrotsky A. Heat capacities, standard entropies and Gibbs energies of Sr-, Rb- and Cs-substituted barium aluminotitanate hollandites. J Chem Thermodyn. 2016;93:1–7. https://doi.org/10.1016/j.jct.2015.09.019
5. Xu H, Costa GCC, Stanek CR, Navrotsky A. Structural behavior of $Ba_{1.24}Al_{2.48}Ti_{5.52}O_{16}$ hollandite at high temperature: An in situ neutron diffraction study. J Am Ceram Soc. 2015;98(1):255–62. https://doi.org/10.1111/jace.13245
6. Ringwood A, Kesson S, Ware N, Hibberson W, Major A. Safe immobilization of high-level nuclear reactor wastes. Canberra: Australian Academy of Science; 1979.
7. Ringwood AE, Kesson SE, Ware NG, Hibberson W, Major A. Immobilisation of high level nuclear reactor wastes in SYNROC. Nature. 1979;278(5701):219–23. https://doi.org/10.1038/278219a0
8. Malkovsky VI, Yudintsev SV, Ojovan MI, Petrov VA. The influence of radiation on confinement properties of nuclear waste glasses. Sci Technol Nucl Install. 2020;2020:8875723. https://doi.org/10.1155/2020/8875723

9. Amoroso J, Marra JC, Tang M, Lin Y, Chen F, Su D, et al. Melt processed multiphase ceramic waste forms for nuclear waste immobilization. J Nucl Mater. 2014;454(1):12–21. https://doi.org/10.1016/j.jnucmat.2014.07.035

10. Tumurugoti P, Sundaram SK, Misture ST, Marra JC, Amoroso J. Crystallization behavior during melt-processing of ceramic waste forms. J Nucl Mater. 2016;473:178–88. https://doi.org/10.1016/j.jnucmat.2016.02.023

11. Zhao M, Xu Y, Shuller-Nickles L, Amoroso J, Frenkel AI, Li Y, et al. Compositional control of radionuclide retention in hollandite-based ceramic waste forms for Cs-immobilization. J Am Ceram Soc. 2019;102(7):4314–24. https://doi.org/10.1111/jace.16258

12. Zhao M, Russell P, Amoroso J, Misture S, Utlak S, Besmann T, et al. Exploring the links between crystal chemistry, cesium retention, thermochemistry and chemical durability in single-phase $(Ba,Cs)_{1.33}(Fe,Ti)_8O_{16}$ hollandite. J Mater Sci. 2020;55(15):6401–16. https://doi.org/10.1007/s10853-020-04447-3

13. Grote R, Zhao M, Shuller-Nickles L, Amoroso J, Gong W, Lilova K, et al. Compositional control of tunnel features in hollandite-based ceramics: Structure and stability of $(Ba,Cs)_{1.33}(Zn,Ti)_8O_{16}$. J Mater Sci. 2019;54(2):1112–25. https://doi.org/10.1007/s10853-018-2904-1

14. Zhao M, Amoroso JW, Fenker KM, DiPrete DP, Misture S, Utlak S, et al. The effect of cesium content on the thermodynamic stability and chemical durability of $(Ba,Cs)_{1.33}(Al,Ti)_8O_{16}$ hollandite. J Am Ceram Soc. 2020;103(12):7310–21. https://doi.org/10.1111/jace.17422

15. Zhao M. An investigation of structure, thermochemistry, electrochemistry, and stability of tunnel structured hollandite materials. Clemson (SC): Clemson University; 2021.

https://www.proquest.com/docview/2540696384/abstract/BF34BFEE260842D7PQ/1 (accessed August 26, 2021)

16. Carter ML, Vance ER, Li H. Hollandite-rich ceramic melts for the immobilisation of Cs. MRS Proceedings. Cambridge University Press; 2003;807:249. https://doi.org/10.1557/PROC-807-249
17. Amoroso J, Marra J, Conradson SD, Tang M, Brinkman K. Melt processed single phase hollandite waste forms for nuclear waste immobilization: $Ba_{1.0}Cs_{0.3}A_{2.3}Ti_{5.7}O_{16}$; A=Cr, Fe, Al. J Alloys Compd. 2014;584:590–9. https://doi.org/10.1016/j.jallcom.2013.09.087
18. Tumurugoti P, Sundaram SK, Brinkman KS, Amoroso JW, Fox KM. Melt-processed multiphasic ceramic waste forms. In: Ohji T, Matyáš J, Manjooran NJ, Pickrell G, Jitianu A, editors. Advances in Materials Science for Environmental and Energy Technologies III. Hoboken: John Wiley & Sons, 2014;250:205–12. https://doi.org/10.1002/9781118996652.ch18
19. Navrotsky A. Progress and new directions in calorimetry: A 2014 perspective. J Am Ceram Soc. 2014;97(11):3349–59. https://doi.org/10.1111/jace.13278
20. Navrotsky A. Progress and new directions in high temperature calorimetry revisited. Phys Chem Miner. 1997;24(3):222–41. https://doi.org/10.1007/s002690050035
21. ASTM International. C1285-14 Standard test methods for determining chemical durability of nuclear, hazardous, and mixed waste glasses and multiphase glass ceramics: The product consistency test (PCT). West Conshohocken: ASTM International; 2014.
22. Zhang J, Burnham CW. Hollandite-type phases: Geometric consideration of unit-cell size and symmetry. Am Mineral. 1994;79(1–2):168–74.

23. Shannon RD. Revised effective ionic radii and systematic studies of interatomic distances in halides and chalcogenides. Acta Crystallogr A. 1976;32(5):751–67. https://doi.org/10.1107/S0567739476001551

24. Bursill LA, Grzinic G. Incommensurate superlattice ordering in the hollandites $Ba_xTi_{8-x}Mg_xO_{16}$ and $Ba_xTi_{8-2x}Ga_{2x}O_{16}$. Acta Crystallogr B. 1980;36(12):2902–13. https://doi.org/10.1107/S0567740880010503

25. Pring A, Smith DJ, Jefferson DA. Supercell ordering in a hollandite-type phase: Potassium magnesium antimony oxide. J Solid State Chem. 1983;46(3):373–81. https://doi.org/10.1016/0022-4596(83)90164-0

26. Mijlhoff FC, IJdo DJW, Zandbergen HW. Constitution and structure of synthetic hollandites, an electron and X-ray diffraction study. Acta Crystallogr B. 1985;41(2):98–101. https://doi.org/10.1107/S0108768185001707

27. Aubin-Chevaldonnet V, Caurant D, Dannoux A, Gourier D, Charpentier T, Mazerolles L, et al. Preparation and characterization of $(Ba,Cs)(M,Ti)_8O_{16}$ ($M = Al^{3+}$, Fe^{3+}, Ga^{3+}, Cr^{3+}, Sc^{3+}, Mg^{2+}) hollandite ceramics developed for radioactive cesium immobilization. J Nucl Mater. 2007;366(1):137–60. https://doi.org/10.1016/j.jnucmat.2006.12.051

28. Carter ML, Withers RL. A universally applicable composite modulated structure approach to ordered $Ba_xM_yTi_{8-y}O_{16}$ hollandite-type solid solutions. J Solid State Chem. 2005;178(6):1903–14. https://doi.org/10.1016/j.jssc.2005.03.040

29. Tumurugoti P, Sundaram SK, Misture ST. Cesium immobilization in (Ba,Cr)-hollandites: Effects on structure. J Solid State Chem. 2018;258:72–8. https://doi.org/10.1016/j.jssc.2017.10.008

30. Leligny H, Labbé P, Ledésert M, Raveau B, Valdez C, McCarroll WH. $La_{1.16}Mo_8O_{16}$: A hollandite-related compound with an incommensurate modulated structure. Acta Crystallogr B. 1992;48(2):134–44. https://doi.org/10.1107/S0108768191013101

31. Xu Y, Feygenson M, Page K, Nickles LS, Brinkman KS. Structural evolution in hollandite solid solutions across the A-site compositional range from $Ba_{1.33}Ga_{2.66}Ti_{5.34}O_{16}$ to $Cs_{1.33}Ga_{1.33}Ti_{6.67}O_{16}$. J Am Ceram Soc. 2016;99(12):4100–6. https://doi.org/10.1111/jace.14443

32. Wu X-J, Fujiki Y, Ishigame M, Horiuchi S. Modulation mechanism and disorder structure in hollandite-type crystals. Acta Crystallogr A. 1991;47(4):405–13. https://doi.org/10.1107/S0108767391001435

33. Cheary RW, Squadrito R. A structural analysis of barium magnesium hollandites. Acta Crystallogr B. 1989;45(3):205–12. https://doi.org/10.1107/S0108768188014053

34. Cheary RW. Structural analysis of hollandite $Ba_xTi_{3+2x}Ti_{4+8-2x}O_{16}$ with x = 1.07 and 1.31 from 5 to 500 K. Acta Crystallogr B. 1990;46(5):599–609. https://doi.org/10.1107/S0108768190006449

35. Leinekugel-le-Cocq-Errien AY, Deniard P, Jobic S, Gautier E, Evain M, Aubin V, et al. Structural characterization of the hollandite host lattice for the confinement of radioactive cesium: Quantification of the amorphous phase taking into account the incommensurate modulated character of the crystallized part. J Solid State Chem. 2007;180(1):322–30. https://doi.org/10.1016/j.jssc.2006.10.013

36. Kesson SE, White TJ, Ringwood AE. $[Ba_xCs_y][(Ti, Al)_{3+2x+y}Ti_{4+8-2x-y}]O_{16}$ Synroc-type hollandites I. Phase chemistry. Proc R Soc Lond Math Phys Sci. 1986;405(1828):73–101. https://doi.org/10.1098/rspa.1986.0042

37. Xu Y, Wen Y, Grote R, Amoroso J, Shuller Nickles L, Brinkman KS. A-site compositional effects in Ga-doped hollandite materials of the form $Ba_xCs_yGa_{2x+y}Ti_{8-2x-y}O_{16}$: Implications for Cs immobilization in crystalline ceramic waste forms. Sci Rep. 2016;6(1):27412. https://doi.org/10.1038/srep27412

38. Robie RA, Hemingway BS. Thermodynamic properties of minerals and related substances at 298.15 K and 1 bar (10^5 Pascals) pressure and at higher temperatures. Washington: United States Government Printing Office; 1995.

39. Lide DR, editor. CRC handbook of chemistry and physics. 85th ed. Boca Raton: CRC press; 2004.

40. Ushakov SV, Navrotsky A, Farmer JM, Boatner LA. Thermochemistry of the alkali rare-earth double phosphates, $A_3RE(PO_4)_2$. J Mater Res. 2004;19(7):2165–75. https://doi.org/10.1557/JMR.2004.0283

41. Hayun S, Navrotsky A. Formation enthalpies and heat capacities of rear earth titanates: RE_2TiO_5 (RE=La, Nd and Gd). J Solid State Chem. 2012;187:70–4. https://doi.org/10.1016/j.jssc.2011.12.033

42. Xu H, Wu L, Zhu J, Navrotsky A. Synthesis, characterization and thermochemistry of Cs-, Rb- and Sr-substituted barium aluminium titanate hollandites. J Nucl Mater. 2015;459:70–6. https://doi.org/10.1016/j.jnucmat.2015.01.014

43. Costa GCC, Xu H, Navrotsky A. Thermochemistry of barium hollandites. J Am Ceram Soc. 2013;96(5):1554–61. https://doi.org/10.1111/jace.12224

44. Speight JG, editor. Lange's handbook of chemistry. 17th ed. New York: McGraw-Hill Education; 2017.

45. Wen Y, Xu Y, Brinkman KS, Shuller-Nickles L. Atomistic scale investigation of cation ordering and phase stability in Cs-substituted $Ba_{1.33}Zn_{1.33}Ti_{6.67}O_{16}$, $Ba_{1.33}Ga_{2.66}Ti_{5.67}O_{16}$ and $Ba_{1.33}Al_{2.66}Ti_{5.33}O_{16}$ hollandite. Sci Rep. 2018;8(1):5003. https://doi.org/10.1038/s41598-018-22982-7

46. Szenknect S, Finkeldei S, Brandt F, Ravaux J, Odorico M, Podor R, et al. Monitoring the microstructural evolution of $Nd_2Zr_2O_7$ pyrochlore during dissolution at 90 °C in 4 M

HCl: Implications regarding the evaluation of the chemical durability. J Nucl Mater. 2017;496:97–108. https://doi.org/10.1016/j.jnucmat.2017.09.029

47. Yang K, Wang Y, Lei P, Yao T, Zhao D, Lian J. Chemical durability and surface alteration of lanthanide zirconates ($A_2Zr_2O_7$: A = La-Yb). J Eur Ceram Soc. 2021;41(12):6018–28. https://doi.org/10.1016/j.jeurceramsoc.2021.05.038
48. Zhao M, O'Quinn E, Birkner N, Xu Y, Lang M, Brinkman K. Radiation damage and thermal annealing in tunnel structured hollandite materials. Acta Mater. 2021;206:116598. https://doi.org/10.1016/j.actamat.2020.116598
49. Yang K, Zhu W, Riley BJ, Vienna JD, Zhao D, Lian J. Perovskite-derived Cs_2SnCl_6–silica composites as advanced waste forms for chloride salt wastes. Environ Sci Technol. 2021;55(11):7605–14. https://doi.org/10.1021/acs.est.0c07724
50. Lei P. Preparation and performance research of ceramic materials for nuclear waste forms. Xiamen (Fujian); Xiamen University; 2020.
51. Ojovan MI, Lee WE, Kalmykov SN. Chapter 23 - Performance of Wasteform Materials. In: Ojovan MI, Lee WE, Kalmykov SN, editors. An introduction to nuclear waste immobilisation. 3rd ed. Amsterdam: Elsevier, 2019; p. 433–61. https://doi.org/10.1016/B978-0-08-102702-8.00023-6

Figure Captions

Figure 1. (a) Rietveld refinement of the $(Ba_xCs_y)(Cr_{2x+y}Ti_{8-2x-y})O_{16}$ hollandite samples with data collected using Cu Kα radiation. Data are plotted as square root of intensity to highlight compositional differences in the superstructure ordering. (b) Rietveld refinement of $Ba_1Cs_{0.3}Cr_{2.3}Ti_{5.7}O_{16}$ with data collected at the 11-ID-B beamline at the Advanced Photon Source using 0.143 Å wavelength radiation. (c) the average ionic radius of A-sites (R_A) and

B-sites (R_B) cations of the Zn, Ga, Fe, Al, and Cr hollandite series. The dashed line is referred to Zhang and Burnham's model for hollandite systems where tetragonal symmetry is expected above the dashed line.[11–14, 22] Note: Ycalc is the calculated intensity from the hollandite atomic model, A-site mod is the calculated intensity from the A-site superstructure, Diff is the difference between experimental and calculated data, Rwp is the residual weight percent, GOF is the goodness of fit, Q is the scattering vector.

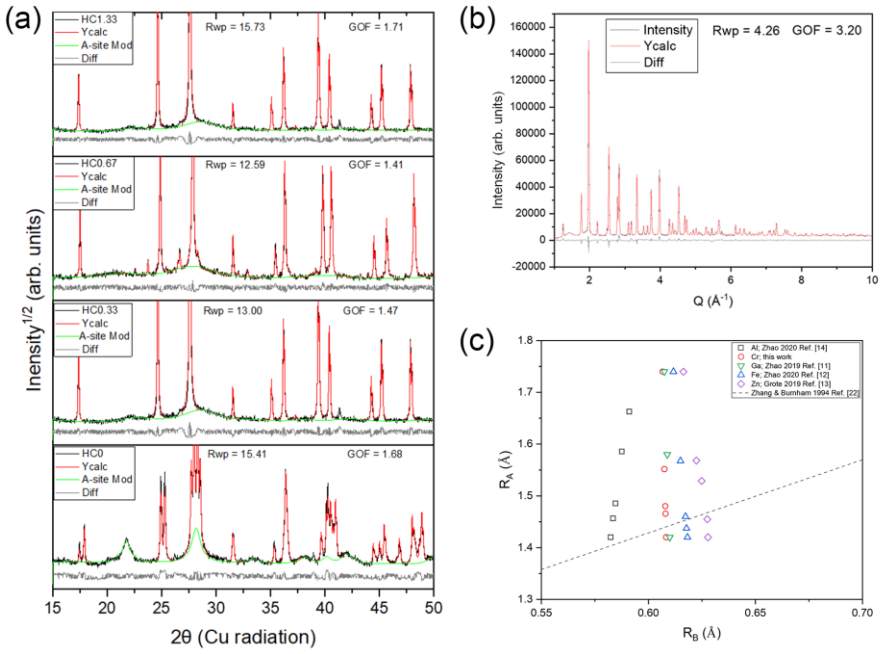

Figure 2. The microstructure of Cr-substituted hollandite samples: (a) HC0, (b) HC0.33, (c) HC0.67, and (d) HC1.33. The scale bar is 10 µm for each composition. Note- SEM images of CU samples looked similar.

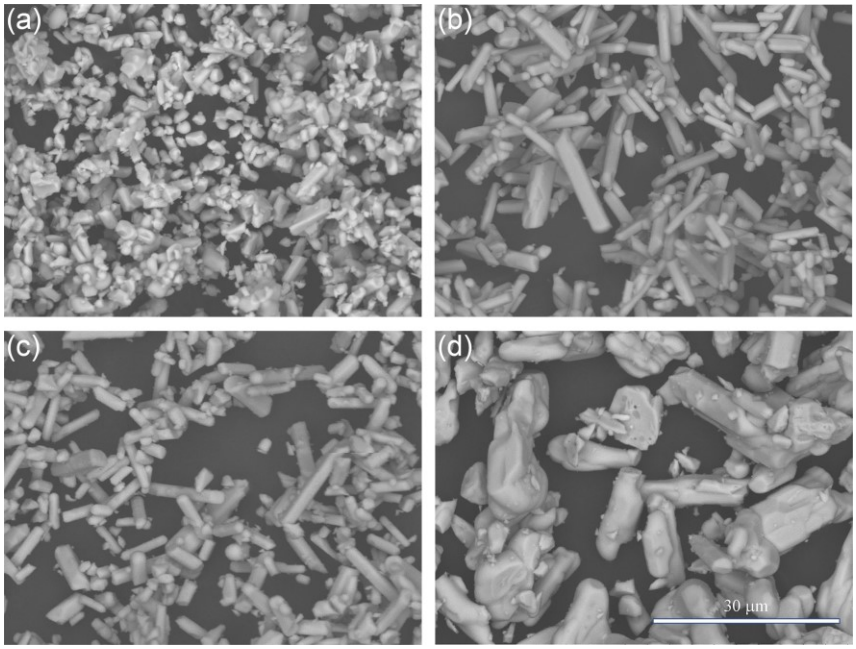

Figure 3. Variations of $\Delta H_{f,ox}$ as a function of Cs content for various hollandite systems with different substitutions.[11–15]

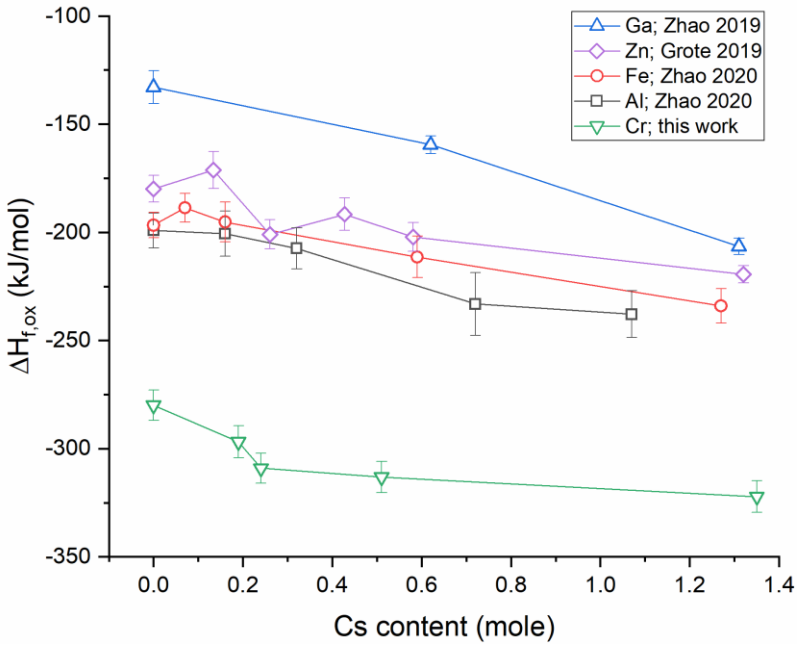

Figure 4. The averaged fractional Cs release (FR_{Cs}) from compacted powder (blue) and sintered pellets (orange). The averaged FR_{Cs} values of the replicates are reported in the form of a histogram. Note: The Cs content is based on nominal stoichiometry.

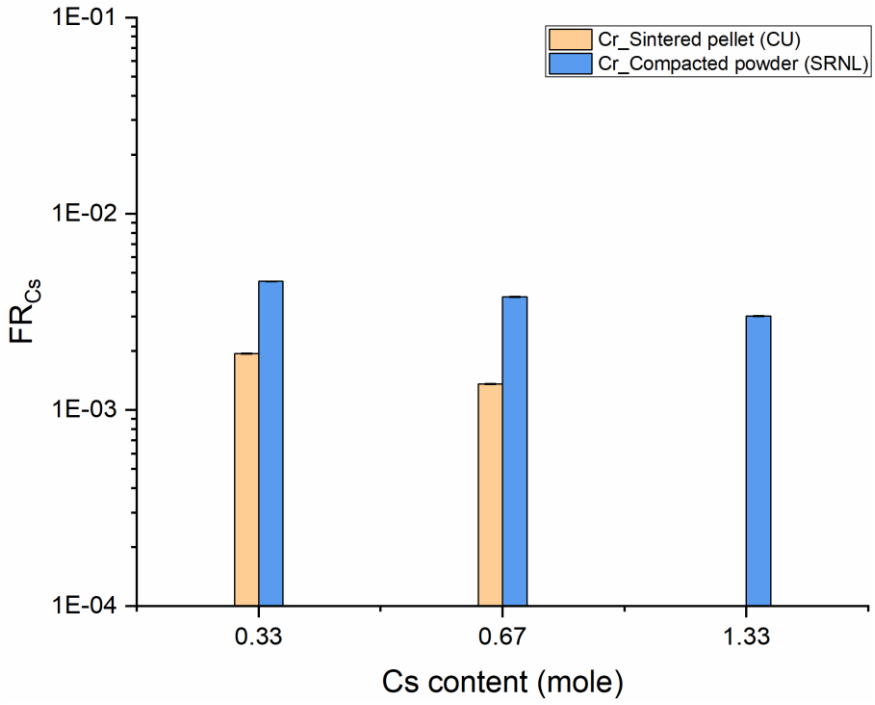

Figure 5. Fractional release (FR) of (a) Cs, (b) Ba, and (c) B-site substitutions for the Cr-, Ga-, Fe-, Al-, and Zn-substituted hollandite samples. The ARM value is reported for comparison. The averaged FR values of the replicates are reported, and the error bars indicate the minimum and maximum measured values. Note: The Cs content is based on nominal stoichiometry.[11–15]

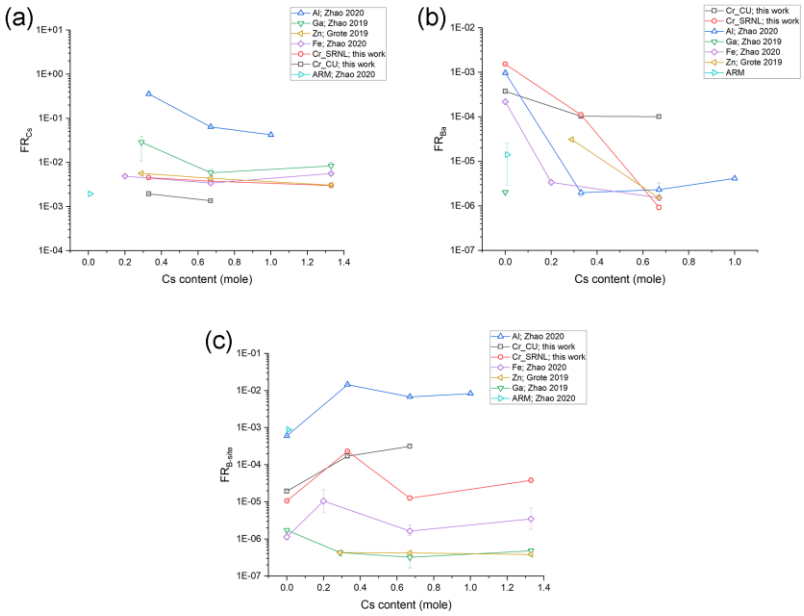

Figure 6. Various ratios of measured elemental release (a) Cs/B-site cation, (b) Ba/B-site cation, and (c) Cs/Ba after seven days of leaching. Note: the dashed bars indicate the stoichiometric ratios between different elements.[11–15]

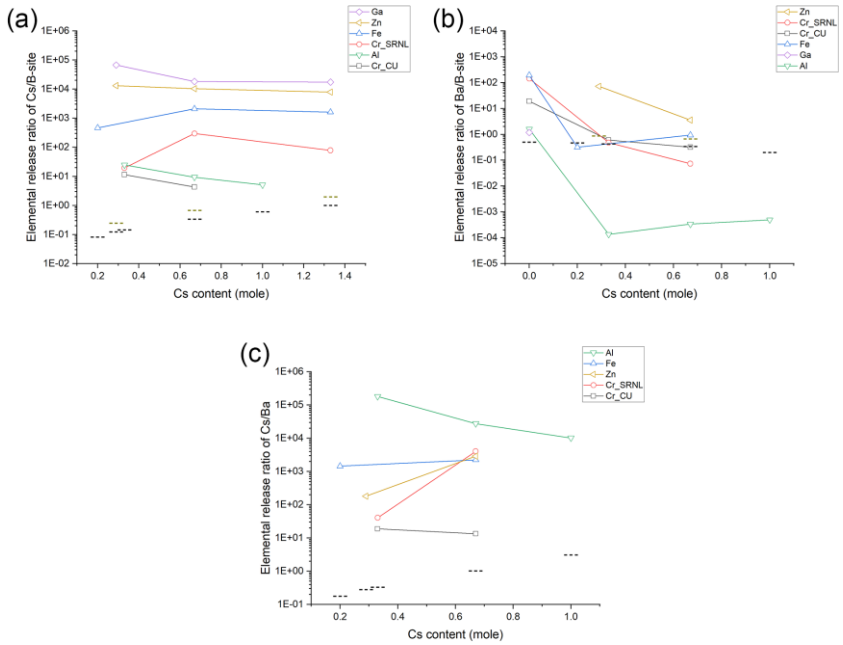

Table Captions

Table 1. Target and Energy Dispersive Spectroscopy (EDS) measured compositions of the Cr-substituted hollandite samples*.

Table 2. Lattice information of the $(Ba_xCs_y)(Cr_{2x+y}Ti_{8-2x-y})O_{16}$ hollandite samples.

Table 3. A-site lattice information where b_f and b_a are the lattice parameters of the framework and A-site along the tunnel direction and x and y the stoichiometric values of Ba and Cs, respectively.

Table 4. The general form of the thermochemical cycle applied with the EDS analyzed stoichiometry of each $(Ba_xCs_y)(Cr_{2x+y}Ti_{8-2x-y})O_{16}$ hollandite sample to calculate the enthalpy of formation from constituent oxides and elements at 25 °C.

Table 5. Measured mean ΔH_{ds} for the Cr-substituted hollandite samples in sodium molybdate solvent at 800 °C and summary of the enthalpies of formation from the binary constituent oxides and the elements at 25 °C.

Tables

Table 1. Target and Energy Dispersive Spectroscopy (EDS) measured compositions of the Cr-substituted hollandite samples*.

Sample name	Target composition	EDS composition
HC0	$Ba_{1.33}Cr_{2.66}Ti_{5.34}O_{16}$	$Ba_{1.29}Cr_{2.69}Ti_{5.34}O_{16}$
HC0.2	$Ba_{1.13}Cs_{0.2}Cr_{2.46}Ti_{5.54}O_{16}$	$Ba_{1.15}Cs_{0.19}Cr_{2.45}Ti_{5.54}O_{16}$
HC0.33	$Ba_{1}Cs_{0.33}Cr_{2.33}Ti_{5.67}O_{16}$	$Ba_{1.04}Cs_{0.24}Cr_{2.34}Ti_{5.67}O_{16}$
HC0.67	$Ba_{0.67}Cs_{0.67}Cr_{2}Ti_{6}O_{16}$	$Ba_{0.73}Cs_{0.51}Cr_{2.01}Ti_{6}O_{16}$
HC1.33	$Cs_{1.33}Cr_{1.33}Ti_{6.67}O_{16}$	$Cs_{1.35}Cr_{1.32}Ti_{6.67}O_{16}$

* Compositions were normalized to Ti with fixed oxygen content to achieve charge balance.

Table 2. Lattice information of the $(Ba_xCs_y)(Cr_{2x+y}Ti_{8-2x-y})O_{16}$ hollandite samples.

Sample	Space Group	a (Å)	b (Å)	c (Å)	β (°)	V_{cell} (Å^3)
HC0	*I*2/*m*	10.1364(4)	2.9538(1)	9.9225(4)	90.744(4)	297.07(2)
HC0.2	*I*4/*m*	10.0568(9)	10.0568(9)	2.9534(2)	90	298.71(6)
HC0.33	*I*4/*m*	10.0756(1)	10.0756(1)	2.9535(4)	90	299.842(9)
HC0.67	*I*4/*m*	10.1412(9)	10.1412(9)	2.9551(1)	90	303.90(2)
HC1.33	*I*4/*m*	10.2434(5)	10.2434(5)	2.9581(1)	90	310.40(3)

Table 3. A-site lattice information where b_f and b_a are the lattice parameters of the framework and A-site along the tunnel direction and x and y the stoichiometric values of Ba and Cs, respectively.

Sample	b_f (Å)	b_a (Å)	Modulation vector γ	$x + y$ (From Eq. 4)	$x + y$ (From EDS*)	A-site crystallite size (Å)
HC0	2.9538(1)	4.57(1)	0.355	1.29	1.29	89
HCO.33	2.9535(4)	4.68(2)	0.369	1.26	1.28	28
HC0.67	2.9551(1)	4.79(4)	0.383	1.23	1.24	17
HC1.33	2.9581(1)	4.25(4)	0.305	1.38	1.35	26

* The sum of $x + y$ is based on the EDS composition in Table 1.

Table 4. The general form of the thermochemical cycle applied with the EDS analyzed stoichiometry of each $(Ba_xCs_y)(Cr_{2x+y}Ti_{8-2x-y})O_{16}$ hollandite sample to calculate the enthalpy of formation from constituent oxides and elements at 25 °C.

Enthalpy of formation from constituent oxides ($\Delta H_{f,ox}$) and elements ($\Delta H_{f,el}$) at 25 °C	ΔH_{ds} (kJ/mol)
$(Ba_xCs_y)(Cr_{2x+y}Ti_{8-2x-y})O_{16(s,\ 25\ °C)} \rightarrow x\ BaO_{(sln,\ 800\ °C)} + 0.5y\ Cs_2O_{(sln,\ 800\ °C)} + 0.5(2x+y)\ Cr_2O_{3(sln,\ 800\ °C)} + (8-2x-y)\ TiO_{2(sln,\ 800\ °C)}$	$\Delta H_1 = \Delta H_{ds}$(Sample)
$BaO_{(s,\ 25\ °C)} \rightarrow BaO_{(sln,\ 800\ °C)}$	$\Delta H_2 = \Delta H_{ds}(BaO)$
$Cs_2O_{(s,\ 25\ °C)} \rightarrow Cs_2O_{(sln,\ 800\ °C)}$	$\Delta H_3 = \Delta H_{ds}(Cs_2O)$
$Cr_2O_{3(s,\ 25\ °C)} \rightarrow Cr_2O_{3(sln,\ 800\ °C)}$	$\Delta H_4 = \Delta H_{ds}(Cr_2O_3)$
$TiO_{2(s,\ 25\ °C)} \rightarrow TiO_{2(sln,\ 800\ °C)}$	$\Delta H_5 = \Delta H_{ds}(TiO_2)$
Calculation of $\Delta H_{f,ox}$ (25 °C)	**$\Delta H_6 = \Delta H_{f,ox}$**
$x\ BaO_{(s,\ 25\ °C)} + 0.5y\ Cs_2O_{(s,\ 25\ °C)} + 0.5(2x+y)\ Cr_2O_{3(s,\ 25\ °C)} + (8-2x-y)\ TiO_{2(s,\ 25\ °C)} \rightarrow$	

$(Ba_xCs_y)(Cr_{2x+y}Ti_{8-2x-y})O_{16(s,\ 25\ °C)}$

$\Delta H_6 = \Delta H_{f,ox} = x\Delta H_2 + 0.5y\Delta H_3 + 0.5(2x+y)\Delta H_4 + (8-2x-y)\Delta H_5 - \Delta H_1$

$x\ BaO_{(s,\ 25\ °C)} + 0.5y\ Cs_2O_{(s,\ 25\ °C)} + 0.5(2x+y)\ Cr_2O_{3(s,\ 25\ °C)} + (8-2x-y)\ TiO_{2(s,\ 25\ °C)} \rightarrow (Ba_xCs_y)(Cr_{2x+y}Ti_{8-2x-y})O_{16(s,\ 25\ °C)}$ $\quad \Delta H_6 = \Delta H_{f,ox}$

$Ba_{(s,\ 25\ °C)} + 0.5\ O_{2(g,\ 25\ °C)} \rightarrow BaO_{(s,\ 25\ °C)}$ $\quad \Delta H_7 = \Delta H_{f,el}(BaO)$

$2\ Cs_{(s,\ 25\ °C)} + 0.5\ O_{2(g,\ 25\ °C)} \rightarrow Cs_2O_{(s,\ 25\ °C)}$ $\quad \Delta H_8 = \Delta H_{f,el}(Cs_2O)$

$2\ Cr_{(s,\ 25\ °C)} + 1.5\ O_{2(g,\ 25\ °C)} \rightarrow Cr_2O_{3(s,\ 25\ °C)}$ $\quad \Delta H_9 = \Delta H_{f,el}(Cr_2O_3)$

$Ti_{(s,\ 25\ °C)} + O_{2(g,\ 25\ °C)} \rightarrow TiO_{2(s,\ 25\ °C)}$ $\quad \Delta H_{10} = \Delta H_{f,el}(TiO_2)$

Calculation of $\Delta H_{f,el}$ (25 °C) $\quad \mathbf{\Delta H_{11} = \Delta H_{f,el}}$

$x\ Ba_{(s,\ 25\ °C)} + y\ Cs_{(s,\ 25\ °C)} + (2x+y)\ Cr_{(s,\ 25\ °C)} + (8-2x-y)\ Ti_{(s,\ 25\ °C)} + 8\ O_{2(g,\ 25\ °C)} \rightarrow (Ba_xCs_y)(Cr_{2x+y}Ti_{8-2x-y})O_{16(s,\ 25\ °C)}$

$\Delta H_{11} = \Delta H_{f,el} = \Delta H_{f,ox} + x\Delta H_7 + 0.5y\Delta H_8 + 0.5(2x+y)\Delta H_9 + (8-2x-y)\Delta H_{10}$

Table 5. Measured mean ΔH_{ds} for the Cr-substituted hollandite samples in sodium molybdate solvent at 800 °C and summary of the enthalpies of formation from the binary constituent oxides and the elements at 25 °C.

Analyzed sample composition	Mean ΔH_{ds} (kJ/mol)	$\Delta H_{f,ox}$ (kJ/mol)	$\Delta H_{f,el}$ (kJ/mol)
$Ba_{1.29}Cr_{2.69}Ti_{5.34}O_{16}$	464.61 ± 5.95 (14)	–280.97 ± 7.22	–7555.15 ± 14.33
$Ba_{1.15}Cs_{0.19}Cr_{2.45}Ti_{5.54}O_{16}$	487.29 ± 6.25 (10)	–297.99 ± 7.32	–7580.94 ± 13.60
$Ba_{1.04}Cs_{0.24}Cr_{2.34}Ti_{5.67}O_{16}$	519.37 ± 5.78 (8)	–310.10 ± 6.82	–7601.73 ± 12.98
$Ba_{0.73}Cs_{0.51}Cr_{2.01}Ti_6O_{16}$	554.81 ± 6.08 (8)	–314.06 ± 6.84	–7606.77 ± 11.98
$Cs_{1.35}Cr_{1.32}Ti_{6.67}O_{16}$	596.46 ± 6.26 (12)	–323.68 ± 6.87	–7599.50 ± 10.34
$BaCO_3$	128.84 ± 1.52 (5)	–271.4 ± 2.10	–1213.0[a]
Cs_2CO_3	97.65 ± 0.76 (5)	–400.2 ± 1.20	–1139.7[a]

BaO	–179.97 ± 2.59	-	–548.1 ± 2.1[b]
Cs_2O	–339.96 ± 1.42	-	–346.0 ± 1.2[b]
Cr_2O_3	16.54 ± 0.83[c]	-	–1134.7 ± 8.4[b]
TiO_2 (rutile)	73.70 ± 0.39[d]	-	–944.0 ± 0.8[b]

[a] CRC Handbook of Chemistry and Physics.[39] [b] Robie and Hemingway.[38] [c] Navrotsky.[19] [d] Hayun and Navrotsky.[41]